



AMERICAN METEOROLOGICAL SOCIETY

Bulletin of the American Meteorological Society

EARLY ONLINE RELEASE

This is a preliminary PDF of the author-produced manuscript that has been peer-reviewed and accepted for publication. Since it is being posted so soon after acceptance, it has not yet been copyedited, formatted, or processed by AMS Publications. This preliminary version of the manuscript may be downloaded, distributed, and cited, but please be aware that there will be visual differences and possibly some content differences between this version and the final published version.

The DOI for this manuscript is doi: 10.1175/BAMS-D-15-00301.1

The final published version of this manuscript will replace the preliminary version at the above DOI once it is available.

If you would like to cite this EOR in a separate work, please use the following full citation:

Zhao, K., M. Wang, M. Xue, P. Fu, Z. Yang, X. Chen, Y. Zhang, W. Lee, F. Zhang, Q. Lin, and Z. Li, 2016: Doppler radar analysis of a tornadic miniature supercell during the Landfall of Typhoon Mujigae (2015) in South China. *Bull. Amer. Meteor. Soc.* doi:10.1175/BAMS-D-15-00301.1, in press.



1 **Doppler radar analysis of a tornadic miniature supercell during**
2 **the Landfall of Typhoon Mujigae (2015) in South China**
3

4 Kun Zhao*¹, Mingjun Wang¹, Ming Xue^{1,2}, Peiling Fu¹,
5 Zhonglin Yang¹, Xiaomin Chen¹ and Yi Zhang¹

6 ¹Key Lab of Mesoscale Severe Weather/Ministry of Education of China,
7 and School of Atmospheric Sciences, Nanjing University, Nanjing,
8 China

9 ²Center for Analysis and Prediction of Storms and School of Meteorology,
10 University of Oklahoma, Norman Oklahoma 73072, USA

11
12 Wen-Chau Lee

13 Earth Observing Laboratory, National Center for Atmospheric Research¹
14 Boulder, Colorado

15
16 Fuqing Zhang

17 Department of Meteorology and Atmospheric Science, and Center for
18 Advanced Data Assimilation and Predictability Techniques, the
19 Pennsylvania State University, University Park, Pennsylvania

20
21 Qing Lin and Zhaohui Li

22 Guangdong Meteorological Observatory, and Foshan tornado research
23 Center, Guangdong Meteorological Service, Guangzhou, China

24
25
26 28 June 2016

27 Submitted to Bulletin of the American Meteorological Society

28 Revised December 8, 2016

29
30
31 *Corresponding author address:

32 Dr. Kun Zhao

33 Key Laboratory of Mesoscale Severe Weather/MOE,
34 School of Atmospheric Sciences, Nanjing University,
35 163 Xianlin Road, Nanjing 210023, China

36 zhaokun@nju.edu.cn
37

1 National Center for Atmospheric Research is sponsored by the National Science Foundation.

Abstract

38

39 On 4 October 2015, a miniature supercell embedded in an outer rainband of
40 Typhoon Mujigae produced a major tornado in Guangdong Province of China, leading
41 to 4 deaths and up to 80 injuries. This study documents the structure and evolution of
42 the tornadic miniature supercell using coastal Doppler radars, a sounding, videos and
43 damage survey. This tornado is rated at least EF3 on the enhanced Fujita scale, and is
44 by far the strongest typhoon rainband tornado yet documented in China and possesses
45 double funnels near its peak intensity.

46 Radar analysis indicates that this tornadic miniature supercell exhibited
47 characteristics similar to those found in US landfalling hurricanes, including hook
48 echo, low-level inflow notches, echo top below 10 km, small and shallow
49 mesocyclone, and long lifespan (~3 h). The environmental conditions consisted of
50 moderate CAPE, low lifted condensation level, small surface dewpoint depression,
51 large veering low-level vertical wind shear, and large cell-relative helicity that are
52 favorable for producing miniature supercells. The mesocyclone, with its maximum
53 intensity at ~2 km above ground level, formed an hour before tornadogenesis. A
54 tornado vortex signature (TVS) was identified between 1 and 3 km AGL, when the
55 parent mesocyclone reached its peak radar-indicated intensity of 30 m s^{-1} . The TVS
56 was located between the updraft and forward-flank downdraft, near the center of the
57 mesocyclone. Dual-Doppler wind analysis reveals that tilting of low-level vorticity
58 into the vertical direction and subsequent stretching by a strong updraft were the main
59 contributors to the mesocyclone intensification.

60

61 **1. Introduction**

62 Tropical cyclone (TC)-spawned tornadoes often occur in the outer rainbands
63 located in the right-front or the northeast quadrant relative to the TC track within a
64 200-400 km annulus (Edwards 2012; Schultz and Cecil 2009). These tornadoes often
65 reside in miniature supercells in an environment characterized by high low-level
66 moisture content, low lifted condensation level, small surface dewpoint depression,
67 small or moderate convective available potential energy (CAPE), and enhanced
68 low-level shear due to increased surface friction from water to land as well as
69 boundary layer convergence (Green et al. 2011). Generally, these miniature supercells
70 exhibit hook echo/appendages and tornado vortex signatures (TVS) in Doppler radar
71 observations (Mccaul 1987; Mccaul et al. 2004). Rare dual-Doppler observations (e.g.,
72 Eastin et al. 2009; Lee et al. 2008) have provided snapshots of the kinematic and
73 dynamic structures of miniature supercells in the United States (US) in the past. In
74 Asia, TC-spawned tornadoes and their parent miniature supercells have been observed
75 by single Doppler radars in Japan and China (e.g. Saito et al. 1992; Suzuki et al. 2000;
76 Zheng et al. 2015), revealing similar radar signatures as in their US counterparts. In
77 China, the average annual number of tornadoes over the past half a century is fewer
78 than 100, and the number of the EF3 (enhanced Fujita scale) intensity or higher
79 tornadoes is ~20 (Fan and Yu 2015). Typhoon rainband spawned tornadoes occurred
80 about once per year in China (Zheng et al. 2015). Nevertheless, the evolution,

81 three-dimensional structures and other dynamic characteristics of miniature supercells
82 in Asia have yet to be documented through dual-Doppler wind analysis.

83 Typhoon Mujigae (2015) was categorized as a Super typhoon ($> 51 \text{ m s}^{-1}$, Yu et al.
84 (2013)) by the Chinese Meteorological Administration (CMA) near the time of
85 landfall in Guangdong Province at 14:00 LST on 4 October 2015. The maximum
86 sustained surface wind was $\sim 52 \text{ m s}^{-1}$ and the minimum central sea-level pressure
87 (MSLP) was 935 hPa (Fig. 1). Mujigae resulted in 19 deaths and \$3.45 billion losses
88 in China, thus “Mujigae” has been retired by the World Meteorological Organization.
89 After its landfall, Mujigae produced two confirmed tornadoes and one waterspout
90 within three separate miniature supercells in the two outermost rainbands (Fig. 1). The
91 strongest tornado, spawned in the third rainband from the center, was located ~ 350
92 km northeast (pole-relative quadrant) of Mujigae’s center and was rated EF3, causing
93 4 deaths, up to 80 injuries, and about \$29 million damages in the city of Foshan.
94 These outer rainbands were accompanied by active lightning over the ocean but
95 lightning activities diminished over land. There were several weak lightning flashes
96 recorded near the Foshan tornadic mini-supercell, but no hail was reported. No
97 tornado warnings were issued, as CMA is currently in the process of establishing a
98 formal tornado warning protocol in China (Xue et al. 2016). Doppler radar data were
99 collected from Guangzhou (GZ) and Shenzhen (SZ) over a 90-min period while the
100 target miniature supercell was located in the western dual-Doppler lobe (Fig. 1). The
101 purpose of this study is to document, for the first time, the time evolution of the

102 strongest TC-spawned tornado ever observed by modern instruments in China, as well
103 as the evolution and structure of the parent mesocyclone and miniature supercell. The
104 paper also compares and contrasts the characteristics of the parent mesocyclone of
105 this TC-spawned tornado with its US counterparts using the Doppler radar data from
106 the closer GZ radar, while coarser-resolution dual-Doppler wind analyses are used to
107 examine the intensification mechanisms of the mesocyclone via vorticity budget
108 analyses.

109 **2. Environmental conditions and damage survey**

110 The environmental conditions of the TC miniature supercell are shown in Fig. 2,
111 based on a rawinsonde released outside the tornadic rainband at the Hong Kong
112 International Airport at 0600 UTC (1400 LST, all times hereafter are LST), about 100
113 km southeast and an hour before the miniature supercell became tornadic. The key
114 buoyancy and shear parameters (Fig. 2), including a moderate CAPE ($\sim 1284 \text{ J kg}^{-1}$),
115 low lifted condensation level ($\sim 389 \text{ m}$), small surface dewpoint depression ($\sim 3 \text{ K}$),
116 large veering low-level (0-3 km) vertical wind shear ($\sim 22.3 \text{ ms}^{-1}$), and large
117 cell-relative helicity ($\sim 211 \text{ m}^2\text{s}^{-2}$), meet the “high threat” category of a TC-spawned
118 tornado in the US (Mccaul 1991; Schneider and Sharp 2007)

119 Damage surveys were conducted jointly by CMA, Nanjing University and
120 Peking University. Aerial photography along the damage path (Fig. 3) was taken by
121 an unmanned aerial vehicle operated by the Foshan Meteorological Bureau during 8 –
122 10 October. Ground damage surveys were also conducted to mark the directions of

123 fallen walls, trees, and power poles. The wind speed estimates of the matched degree
124 of damage (DOD) were assigned the expected values (EXP in McDonald and Mehta
125 2006) for all of the damage indicators (DIs) (Meng and Yao 2014). Visual evidences
126 (e.g., photographs and videos) of the tornado were also collected from a variety of
127 sources (e.g., from news websites and a variety of online social media, etc.), which
128 provided photographic evidence of the tornado. The most severe damages were rated
129 EF3 as recommended by the Wind Science and Energy Center (McDonald and Mehta
130 2006).

131 The tornado's damage track was about 30 km long (Fig. 3c, white line). The
132 wind damage first appeared to the southeast of LD, but without clear tornado damage
133 patterns. The tornado's parent supercell moved NNW with a mean speed $\sim 21 \text{ m s}^{-1}$. At
134 LY, a funnel cloud was captured by a cellphone camera at ~ 153124 (Fig. 3a) by Mr. S.
135 Huang (available on youku.com), suggesting that the tornado touched down between
136 LD and LY. Ten seconds later at 153134, two funnels are apparent (Fig. 3e). Several
137 factory buildings were completely demolished by the tornado between LD and LY,
138 within a damage swath $\sim 150 \text{ m}$ (Fig. 3b). The DI of this steel frame building with
139 DOD 8 was rated EF3. The tornado then hit SB at ~ 1534 and damaged a larger group
140 of steel frame buildings (rated EF3, not shown). A concrete electrical transmission
141 line pole was snapped (Fig. 3d) north of MD (rated EF3). The tornado maintained
142 high intensity while broadening, and reached its widest damage path ($\sim 500 \text{ m}$) at YB
143 with the same DOD as those in LY and SB.

144 **3. Radar signatures of the miniature supercell, mesocyclone and tornado**

145 **3.1 Miniature supercell and mesocyclone**

146 The damage track matched well with the “hook echo” radar reflectivity signature
147 and the accompanying Doppler velocity dipole where V_{\max} and V_{\min} are the outbound
148 and inbound Doppler velocity maxima (Fig. 4). A mesocyclone usually possesses a
149 diameter between 2 to 10 km and a vertical vorticity on the order of 0.01 s^{-1} or greater
150 (American Meteorological Society 2016). Figure 5 illustrates the characteristics of the
151 mesocyclone from the estimated axisymmetric rotational velocity, $V_{\text{rot}} = (V_{\max} -$
152 $V_{\min})/2$, and the mesocyclone diameter, D , defined as the distance between V_{\max} and
153 V_{\min} (Lee and White 1998; Stumpf et al. 1998), and azimuthal shear (one half of the
154 vorticity), $(V_{\max} - V_{\min})/D$. The cyclonic vortex associated with the tornado-producing
155 miniature supercell (Fig. 5) easily met the criteria of a mesocyclone (Andra 1997; Lee
156 and White 1998) with a vorticity exceeding 10^{-2} s^{-1} at 1430 and ~ 3 km above ground
157 level (AGL, hereafter all heights are AGL). The mesocyclone rapidly intensified
158 below 3 km altitude with a $V_{\text{rot}} \sim 30 \text{ m s}^{-1}$ at 1530. It can be categorized as a strong
159 mesocyclone according to the mesocyclone strength nomogram (Andra 1997).
160 Associated with the strengthening of the mesocyclone, its diameter contracted from
161 ~ 6 km to less than 3 km at 1530 when the tornado was observed on the ground with
162 vorticity exceeding $3 \times 10^{-2} \text{ s}^{-1}$. The mesocyclone continued to contract toward $D \sim 2$
163 km at 1542 while V_{rot} peaked ~ 1530 with vorticity exceeding $4.5 \times 10^{-2} \text{ s}^{-1}$. This could
164 be a sign of the mesocyclone intensifying and collapsing into a tornado vortex as

165 documented in Wakimoto et al. (1998). However, the Guangzhou radar's beamwidth
166 (~400 m) was too coarse to resolve the tornado ($D \sim 200$ m) at a distance of ~25 km
167 from the radar. It is noted that the lowest elevation of Guangzhou radar was 0.5° such
168 that the lowest level of the mesocyclone was better sampled as it moved closer to the
169 radar from 1436 to 1546. EF3 tornado damages coincided with the time of peak
170 mesocyclone intensity, consistent with previous studies that ~90% of EF3–EF5
171 tornadoes were associated with strong mesocyclones (e.g, Smith 1965). The
172 mesocyclone weakened and broadened after 1536 (Fig. 5).

173 **3.2 TVS**

174 A TVS is defined as a velocity signature with local maximum and minimum over
175 an azimuthal distance of approximately one beamwidth (< 1 km) and with
176 gate-to-gate azimuthal radial velocity difference (ΔV) greater than 20 m s^{-1} (Brown et
177 al. 1978). The TVS was first detected at 1526 at 2.4° elevation (about 1.2 km) near
178 LD. By ~1530, the TVS intensified rapidly and descended toward the surface (Fig.
179 4b). It could be detected at all elevations below 9.9° except 0.5° (Fig. 5). The lack of a
180 consistent TVS at 0.5° can be attributed to the strong second trip echo contaminating
181 the radial velocities in the TVS region. In fact, the first surface damage was identified
182 near LD ~1528, and a video confirms the tornado was on the ground at approximately
183 1530. From 1530 to 1536, the TVS at all elevations below 3.4° continued to intensify
184 with ΔV greater than 50 m s^{-1} . The strongest TVS was detected at the 0.5° PPI at 1536
185 with a magnitude of $\Delta V \sim 60 \text{ m s}^{-1}$; this was collocated with the severe damage

186 exemplified by the demolished factories near LY. In the next 6 min, the low-level TVS
187 intensity decreased below 55 m s^{-1} . The extreme radar reflectivity ($> 60 \text{ dBZ}$) in the
188 hook echo at 1536 and 1542 also is suggestive of a tornado debris signature (Fig.4c-d).
189 The strongest damage occurred at MD ~ 1540 when a concrete pole with a diameter of
190 0.5 m was snapped (Fig. 3d, and blue dot in Fig.5), supporting an EF3 tornado. After
191 that, the TVS continued to weaken, coincident with the weak damages between JB
192 and QK. From 1600 onwards, the TVS became undetectable in radar data, consistent
193 with the end of the damage pattern north of QK.

194 **4. Kinematic structure of the miniature supercell**

195 Doppler radial velocities from Guangzhou and Shenzhen radars were first
196 interpolated onto a $1 \text{ km} \times 1 \text{ km} \times 1 \text{ km}$ Cartesian grid using the National Center
197 for Atmospheric Research's REORDER software (Oye et al. 1995), then synthesized
198 into 3-D winds using CEDRIC (Mohr et al. 1986). The miniature supercell motion
199 ($\sim 21.7 \text{ m s}^{-1}$ towards an azimuth of 330° relative to true north) was accounted for in
200 the interpolation procedure. Although the Guangzhou radar is closer to the tornado,
201 the scale of the dual-Doppler syntheses is determined by the coarser sampling
202 resolution from the Shenzhen radar $\sim 80 \text{ km}$ from the tornado. As a result, the
203 dual-Doppler syntheses can only resolve the parent mesocyclone and the miniature
204 supercell. The evolution and intensification of the mesocyclone circulation at the
205 southeast end of the miniature supercell are illustrated using the storm-relative wind
206 vectors at 1.5 km and 3.5 km (Fig. 6).

207 The storm-relative velocity field at 1.5 km is dominated by a closed cyclonic
208 circulation (Fig. 6a). The mid-level inflow (Fig. 6d) came from the southwest, and
209 turned cyclonically towards north after it entered the storm. The vorticity maximum is
210 located northeast of the low-level vorticity center, indicating tilting of the low-level
211 horizontal vorticity aligned with the storm motion, consistent with the low-level shear
212 vector as shown in Fig. 3. At 1454 (Fig. 6b, e), the mesocyclone at low levels
213 intensified with its vorticity center collocated with the maximum updraft, as the wind
214 fields in the midlevels became more southerly. Thirty minutes later at 1530 (Fig. 6c,
215 f), the magnitude of the mesocyclone, accompanied by a hook echo, intensified by
216 more than 100% with the vorticity maximum exceeding $2 \times 10^{-2} \text{ s}^{-1}$ and its diameter
217 decreased to less than 5 km (based on the $5 \times 10^{-3} \text{ s}^{-1}$ vorticity contour). The tornado
218 occurred near the center of the cyclonic circulation. Note that the vorticity maximum
219 (i.e., the mesocyclone) is shifted north of the updraft center. The cyclonic circulation
220 is well defined in the midlevels (Fig. 6f).

221 Figure 7 presents two orthogonal vertical cross sections of reflectivity, vertical
222 velocity, and vertical vorticity through the mesocyclone center. The miniature
223 supercell and its mesocyclone extend up to 8 km and 4 km based on the 20 dBZ and 5
224 $\times 10^{-3} \text{ s}^{-1}$ contour, respectively, with the maximum vorticity $\sim 2 \times 10^{-2} \text{ s}^{-1}$ at 2 km.
225 These characteristics are consistent with miniature supercells observed in TC
226 rainbands in the US (e.g, Eastin et al. 2009; Mccaul et al. 2004; Spratt et al. 1997).
227 The storm-relative inflow approaches from the northeast, and the primary updraft

228 extends from the boundary layer up to ~ 6 km with a maximum of ~ 10 m s⁻¹ near 3
229 km altitude. A moderate downdraft with a maximum of ~ 6 m s⁻¹ is confined to the
230 north of the updraft within the inflow region, which can be attributed to the
231 compensating downdraft of the convective updraft and the drag by heavy precipitation
232 (> 45 dBZ). The tornado is located at the boundary between the updraft and
233 downdraft.

234 To examine the intensification mechanism of the mesocyclone in this miniature
235 supercell, the vertical vorticity budget from the 3D dual-Doppler winds is calculated
236 using the method described in Eastin et al. (2009). Ignoring contributions from
237 frictional and solenoidal terms that are usually much smaller, the time rate of change
238 of vertical vorticity can be expressed as the sum of horizontal (HADV) and vertical
239 (VADV) advection of vertical vorticity, the convergence (CONV, or stretching) and
240 tilting (TILT) terms. Figure 8 shows the horizontal distribution of the vertical vorticity
241 production terms at $Z=1.5$ km in the vicinity of the mesocyclone at 1454 and 1530,
242 corresponding to the times before and near tornadogenesis, respectively. At 1454 LST
243 (Fig.8a-d), the CONV term is mostly positive within the mesocyclone. The tilting
244 term is comparable in magnitude to the CONV term, and has positive contributions to
245 the vorticity of the mesocyclone. Both HADV and VADV terms exhibit a pair of
246 positive and negative maxima near the center of the mesocyclone, consistent with the
247 effect of advection by the storm-relative winds and vertical motion. Overall, the

248 low-level vorticity production before tornadogenesis mostly resulted from tilting of
249 horizontal vorticity and its subsequent stretching.

250 Near the time of tornadogenesis ~1530 (Fig.7e-h), CONV and HADV terms
251 increased to an order of magnitude larger than VADV and TILT. The HADV term still
252 exhibits a positive (negative) maximum at the southwest (northeast) flank of the
253 mesocyclone center. Maximum CONV exceeds $25 \times 10^{-6} \text{ s}^{-2}$ and is collocated with
254 the mesocyclone, indicating its dominant role in the production of vertical vorticity.
255 The vorticity distribution and evolution in this event are consistent with supercells
256 found in the US Great Plains, where the vertical vorticity couplet is initially created
257 by tilting of horizontal environmental vorticity, then positive vorticity is rapidly
258 intensified by the stretching of vertical vorticity within the mesocyclone (e.g,
259 Davies-Jones et al. 2001; Mccaul and Weisman 1996).

260 Past studies (e.g.,Dawson et al. 2010; Markowski et al. 2002) have pointed to the
261 importance of the cold pool, including its strength, in tornadogenesis. For the
262 miniature supercell storm studied here, the cold pool was rather weak; the surface
263 temperature drops were less than 1 K at surface stations near the path of the tornado
264 (not shown), which is not surprising because of the very humid low level environment.
265 Hence the baroclinically generated vorticity should not be an important factor.

266 **5. Concluding remarks**

267 The first look of the evolution and structure of a miniature supercell in Typhoon
268 Mujigae (2015), which spawned an EF3 tornado, the strongest tornado embedded in a
269 typhoon rainband ever observed in China, was presented in this paper using single and

270 dual-Doppler radar data along with rawinsonde and damage surveys. The tornadic
271 mini-supercell was embedded in an environment of a moderate CAPE, strong
272 low-level shear, low lifted condensation level and small surface dewpoint depression,
273 similar to its US hurricane counterparts. Mesocyclone properties deduced from
274 single-Doppler radar data suggest that the mesocyclone first intensified and contracted
275 at ~3 km altitude, then descended to lower levels. Due to the limitations of the
276 available data, we are unable to investigate the details of tornadogenesis and the
277 subsequent evolution and structure of the tornado.

278 With dual-Doppler wind analyses, the parent mesocyclone was well identified.
279 Positive vorticity intensified as the hook echo reflectivity signature developed. The
280 vorticity budget demonstrated that tilting of the low-level horizontal vorticity into the
281 vertical and subsequent stretching by strong updraft were the main contributors to the
282 mesocyclone intensification. Future studies will examine the microphysical processes
283 of the miniature supercell using dual-polarization data from the Hong Kong radar. In
284 addition, storm dynamics and tornadogenesis will be examined using high-resolution
285 numerical simulations that include radar data assimilation.

286

287

288

289 **Acknowledgements**

290 This work was primarily supported by the National Fundamental Research 973
291 Program of China (2013CB430100 and 2015CB452801), the National Natural
292 Science Foundation of China (grants 41322032, 41275031 and 41230421), and the
293 Social Commonwealth Research Program (GYHY201006007). We would like to

294 acknowledge the China Meteorological Administration for organizing damage surveys
295 and collecting the radar data used in this study. Special thanks also go to all people
296 who took part in the tornado damage survey and shared their valuable pictures and
297 videos of the tornado damage. We would also like to acknowledge Mr. Huang Sheng
298 who shared his useful videos of the tornado.
299

300 **Reference**

- 301 American Meteorological Society, 2016: *Mesocyclone*. Glossary of Meteorology.
302 [Available online at <http://glossary.ametsoc.org/wiki/Mesocyclone>].
- 303 Andra, D. L., 1997: The origin and evolution of the WSR-88D mesocyclone
304 recognition nomogram. *Conference on Radar Meteorology, 28 th, Austin, TX, 1997*.
- 305 Brown, R. A., L. R. Lemon, and D. W. Burgess, 1978: Tornado detection by pulsed
306 Doppler radar. *Monthly Weather Review*, **106**, 29-38.
- 307 Davies-Jones, R., R. J. Trapp, and H. B. Bluestein, 2001: Tornadoes and tornadic
308 storms. *Severe convective storms*, Springer, 167-221.
- 309 Dawson, D. T., M. Xue, J. A. Milbrandt, and M. Yau, 2010: Comparison of
310 evaporation and cold pool development between single-moment and multimoment
311 bulk microphysics schemes in idealized simulations of tornadic thunderstorms.
312 *Monthly Weather Review*, **138**, 1152-1171.
- 313 Eastin, Matthew D Link, and M. Christopher, 2009: Miniature supercells in an
314 offshore outer rainband of Hurricane Ivan (2004). *Monthly Weather Review*, **137**,
315 2081-2104.
- 316 Edwards, R., 2012: Tropical cyclone tornadoes: A review of knowledge in research
317 and prediction. *E-Journal of Severe Storms Meteorology*, **7**.
- 318 Fan, W., and X. Yu, 2015: Characteristics of Spatial-Temporal Distribution of
319 Tornadoes in China. *Meteorological Monthly*, (in Chinese).
- 320 Green, B. W., F. Zhang, and P. Markowski, 2011: Multiscale processes leading to
321 supercells in the landfalling outer rainbands of Hurricane Katrina (2005). *Weather and*
322 *Forecasting*, **26**, 828-847.
- 323 Lee, R. R., and A. White, 1998: Improvement of the WSR-88D mesocyclone
324 algorithm. *Weather and forecasting*, **13**, 341-351.
- 325 Lee, W. C., M. M. Bell, and K. E. Goodman, 2008: Supercells and mesocyclones in
326 outer rainbands of Hurricane Katrina (2005). *Geophysical Research Letters*, **35**.
- 327 Markowski, P. M., J. M. Straka, and E. N. Rasmussen, 2002: Direct Surface
328 Thermodynamic Observations within the Rear-Flank Downdrafts of Nontornadic and
329 Tornadic Supercells. *Monthly Weather Review*, **130**, 1692-1721.
- 330 Mccaul, E. W., 1987: Observations of the Hurricane ``Danny" Tornado Outbreak of 16
331 August 1985. *Monthly Weather Review*, **115**, 1206.
- 332 —, 1991: Buoyancy and Shear Characteristics of Hurricane-Tornado Environments.
333 *Monthly Weather Review*, **119**, 1954.
- 334 Mccaul, E. W., and M. L. Weisman, 1996: Simulations of Shallow Supercell Storms
335 in Landfalling Hurricane Environments. *Monthly Weather Review*, **124**, 408.
- 336 Mccaul, E. W., D. E. Buechler, S. J. Goodman, and M. Cammarata, 2004: Doppler
337 Radar and Lightning Network Observations of a Severe Outbreak of Tropical Cyclone
338 Tornadoes. *Monthly Weather Review*, **132**, 1747.
- 339 McDonald, J. R., and K. C. Mehta, 2006: *A recommendation for an Enhanced Fujita*
340 *scale (EF-Scale)*. Wind Science and Engineering Center, Texas Tech University.
- 341 Meng, z., and d. Yao, 2014: Damage Survey, Radar, and Environment Analyses on the

342 First-Ever Documented Tornado in Beijing during the Heavy Rainfall Event of 21
343 July 2012. *Weather and Forecasting*, **29**, 702-724.

344 Mohr, C. G., L. Jay Miller, R. L. Vaughan, and H. W. Frank, 1986: The merger of
345 mesoscale datasets into a common Cartesian format for efficient and systematic
346 analyses. *Journal of Atmospheric and Oceanic Technology*, **3**, 143-161.

347 Oye, R., C. Mueller, and S. Smith, 1995: Software for radar translation, visualization,
348 editing, and interpolation. *Preprints, 27th Conf. on Radar Meteorology, Vail, CO,*
349 *American Meteorology Society*, 359-361.

350 Saito, R., M. Fujita, G. Dresselhaus, and M. S. Dresselhaus, 1992: Electronic structure
351 of chiral graphene tubules. *Applied Physics Letters*, **60**, 2204-2206.

352 Schneider, D., and S. Sharp, 2007: Radar signatures of tropical cyclone tornadoes in
353 central North Carolina. *Weather and forecasting*, **22**, 278-286.

354 Schultz, L. A., and D. J. Cecil, 2009: Tropical cyclone tornadoes, 1950-2007. *Monthly*
355 *Weather Review*, **137**, 3471-3484.

356 Smith, J. S., 1965: The hurricane-tornado. *Monthly weather review*, **93**, 53-51.

357 Spratt, S. M., D. W. Sharp, P. Welsh, A. Sandrik, F. Alsheimer, and C. Paxton, 1997: A
358 WSR-88D assessment of tropical cyclone outer rainband tornadoes. *Weather and*
359 *forecasting*, **12**, 479-501.

360 Stumpf, G. J., and Coauthors, 1998: The National Severe Storms Laboratory
361 Mesocyclone Detection Algorithm for the WSR-88D*. *Weather and Forecasting*, **13**,
362 304-326.

363 Suzuki, H., T. ABE, K. Takaishi, M. Narita, and F. Hamada, 2000: New Polyimides
364 Derived from Norbornanetetracarboxylic Dianhydride and Aromatic Diamine
365 Showing Excellent Transparency and Heat-Resistance. *International Journal of the*
366 *Society of Materials Engineering for Resources*, **8**, 9-14.

367 Wakimoto, R. M., C. Liu, and H. Cai, 1998: The Garden City, Kansas, storm during
368 VORTEX 95. Part I: Overview of the storm's life cycle and mesocyclogenesis.
369 *Monthly weather review*, **126**, 372-392.

370 Xue, M., K. Zhao, M. Wang, Z. Li, and Y. Zheng, 2016: Recent significant tornadoes
371 in China. *Advances in Atmospheric Sciences*, **33**, 1209-1217.

372 Yu, H., P. Chen, Q. Li, and B. Tang, 2013: Current Capability of Operational
373 Numerical Models in Predicting Tropical Cyclone Intensity in the Western North
374 Pacific. *Weather and Forecasting*, **28**, 353-367.

375 Zheng, Y., B. Zhang, X. Wang, K. Sun, R. Mu, and W. Xia, 2015: Analysis of
376 typhoon-tornado weather background and radar echo structure. *Meteorological*
377 *Monthly*, **41**, 942-952 (in Chinese with English abstract).

378

379

380 **Figure Captions**

381 **Figure 1.** The radar sites (solid triangles) at Guangzhou (GZ) and Shenzhen (SZ), and
382 the sounding station (white Pentagram) at Hong Kong (HK) are overlaid on the
383 composite reflectivity of tropical cyclone Mujigae at 1500 LST, 4 October, 2015. Two
384 circles indicate the dual-Doppler radar analysis domain. The TC track is the black line
385 segments with TC symbols represent the TC centers every 6 hours, and the black
386 rectangle outlines the region where Foshan tornado occurred. The tornado track is
387 indicated by the thick blue line segment.

388 **Figure 2.** (a) Sounding profile and (b) hodograph at 1400 LST from the Hong Kong
389 Airport. Temperature and dewpoint profiles are represented by black solid lines, while
390 a surface-based parcel path is shown as the black dashed line. The cross-hatched area
391 represents the 1284 J Kg^{-1} CAPE for the lifted parcel. Winds (half barb = 5 m s^{-1} ; full
392 barb = 10 m s^{-1}) are also shown. The grey arrow in (b) represents the storm motion.

393 **Figure 3.** Damage survey of tornado path corresponding to the black rectangle in
394 Fig.1. The visual tornado is viewed from the north and the associated damages are
395 illustrated in (b) and (d).

396 **Figure 4.** Damage survey of tornado path (solid black line) from Fig. 3 and the TVS
397 (black cross) superimposed on radar reflectivity (dBZ) at 1.5° elevation angle from the
398 Guangzhou radar and ground-relative radial velocities (m s^{-1}) from 1524 to 1554 LST
399 at an interval of 6 min.

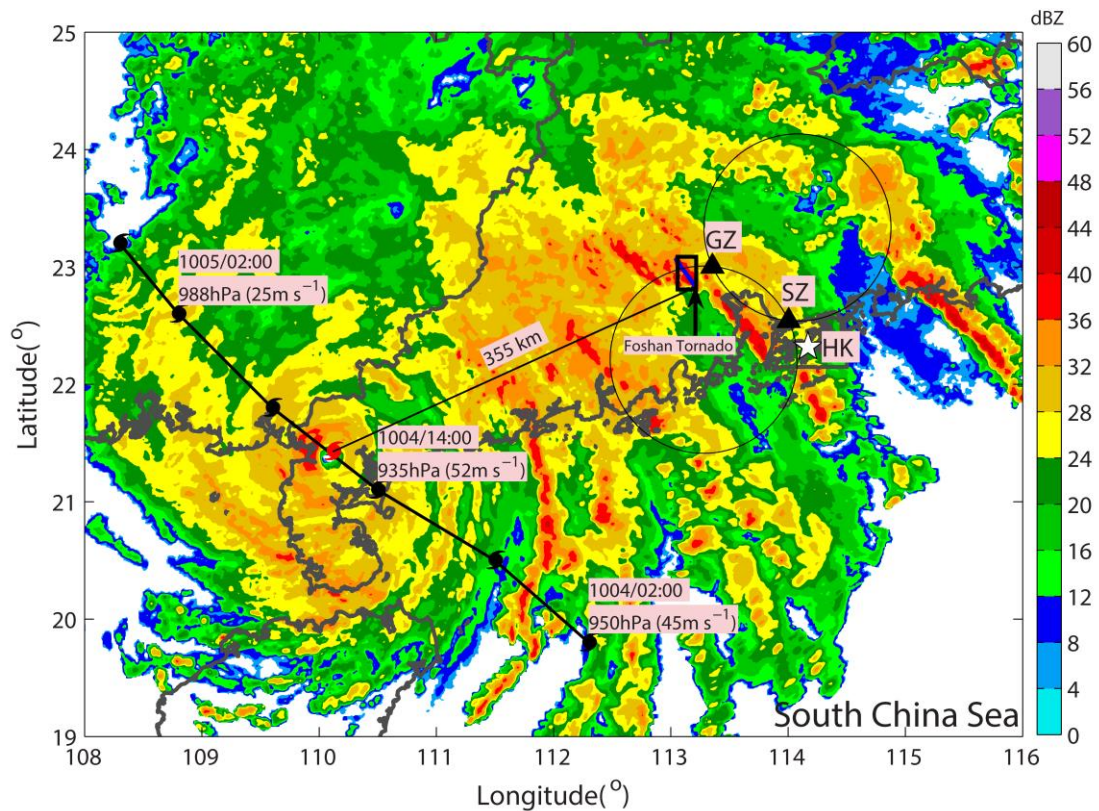
400 **Figure 5.** Time-height profiles of (a) rotational velocity (m s^{-1}), gray lines represent
401 20 and 26 m s^{-1} contours, (b) couplet diameter (km), gray lines represent 3 km
402 contours, and (c) azimuthal shear (10^{-3} s^{-1} , approximately one half of the vertical
403 vorticity) for the tornado's parent mesocyclone, gray lines represent 15 and 20×10^{-3}
404 s^{-1} contours. A distance scale (km) relative to Guangzhou radar along with the local

405 time is indicated on the horizontal axis. The strength of the TVS, defined by the
406 gate-by-gate radial velocity difference is indicated by circles in (a). Colors represent
407 the elevation angle of PPI scan associated with each quantity. The presence of the
408 tornado, through visual and damage track records, is indicated by the red line.

409 **Figure 6.** Dual-Doppler analysis of tornadic mesocyclone from Guangzhou and
410 Shenzhen radars at 1.5 km height (top row) and 3.5 km height (bottom row) at (a,d)
411 1430 LST, (b,e) 1454 LST and (c,f) 1530 UTC, corresponds to before and at the time
412 of tornadogenesis. Reflectivity (color, dBZ) is overlaid with storm-relative wind
413 vectors. The positive (white solid line) and negative (white dashed line) vertical
414 vorticity is contoured at $\pm 1, 5, 10, 15,$ and $20 \times 10^{-3} \text{ s}^{-1}$. The updraft (blue line) is
415 contoured at 2, 4, 6, 8, 10 m s^{-1} . The green filled triangles indicate the location of the
416 TVS.

417 **Figure 7.** Vertical cross sections of radar reflectivity (dBZ, color shading),
418 storm-relative wind vectors, vertical velocity (m s^{-1} , blue contours), and vertical
419 vorticity ($1 \times 10^{-3} \text{ s}^{-1}$, white contours) at 1530 LST (at the time of tornadogenesis)
420 along (a) AB and (b) CD in Fig. 5c. The solid and dashed lines denote
421 positive-negative values, respectively. The green filled triangles indicate the location
422 of TVS.

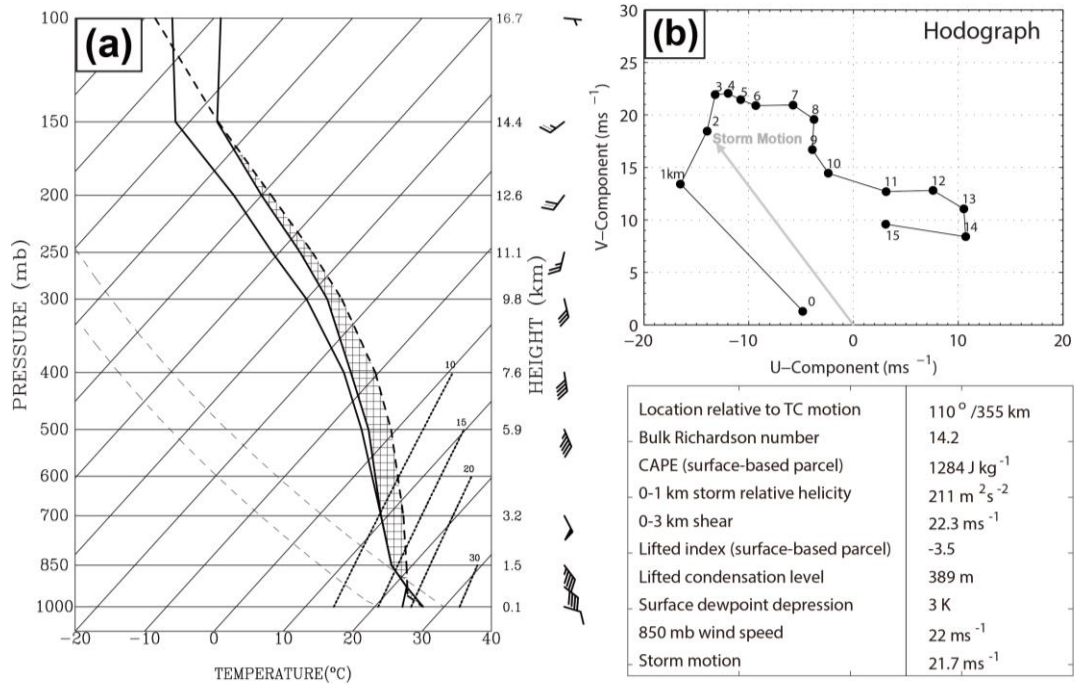
423 **Figure 8.** Distributions of (a,e) HADV, (b,f) VADV, (c,g) TILT, and (d, h) CONV
424 terms within the mesocyclone at 1.5 km at 1454 LST (upper row) and 1530 LST
425 (bottom row), corresponding to the times before and near tornadogenesis. Blue solid
426 (dashed) contours denote positive (negative) contributions to vertical vorticity
427 production with the interval of $2 \times 10^{-6} \text{ s}^{-2}$. Reflectivity (dBZ, color shading) is
428 overlaid with storm-relative wind vectors and vertical relative vorticity (white
429 contours with intervals of $4 \times 10^{-3} \text{ s}^{-1}$).



431

432 **Figure 1.** The radar sites (solid triangles) at Guangzhou (GZ) and Shenzhen (SZ), and
 433 the sounding station (white pentagram) at Hong Kong (HK) are overlaid on the
 434 composite reflectivity of tropical cyclone Mujigae at 1500 LST, 4 October, 2015. Two
 435 circles indicate the dual-Doppler radar analysis domain. The TC track is the black line
 436 segments with TC symbols represent the TC centers every 6 hours, and the black
 437 rectangle outlines the region where Foshan tornado occurred. The tornado track is
 438 indicated by the thick blue line segment.

439



440

441

442 **Figure 2.** (a) Sounding profile and (b) hodograph at 1400 LST from the Hong Kong

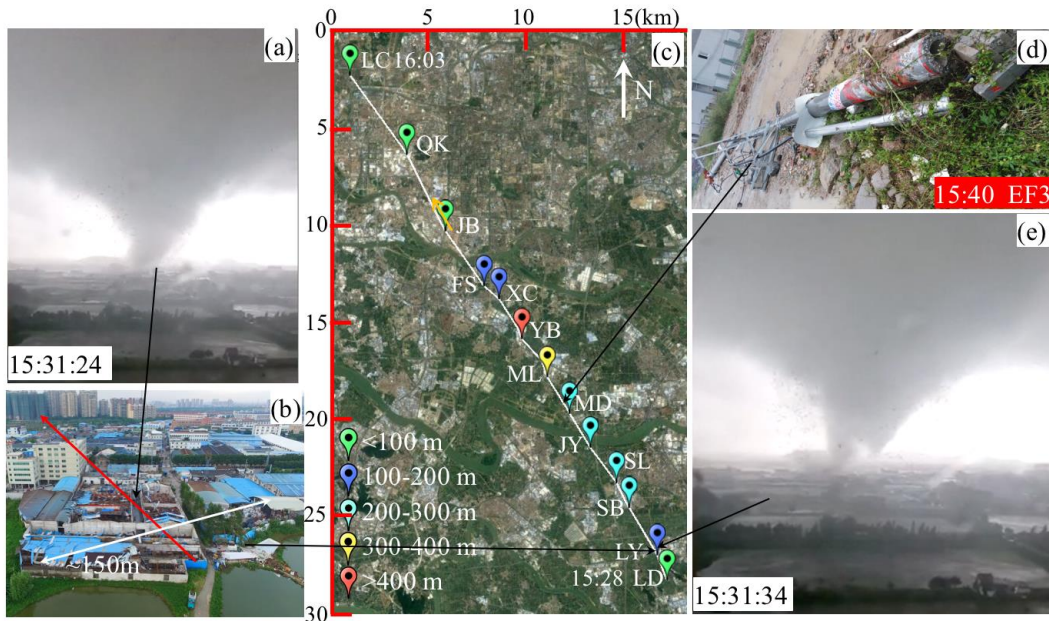
443 Airport. Temperature and dewpoint profiles are represented by black solid lines, while

444 a surface-based parcel path is shown as the black dashed line. The cross-hatched area

445 represents the 1284 J Kg⁻¹ CAPE for the lifted parcel. Winds (half barb = 5 m s⁻¹; full

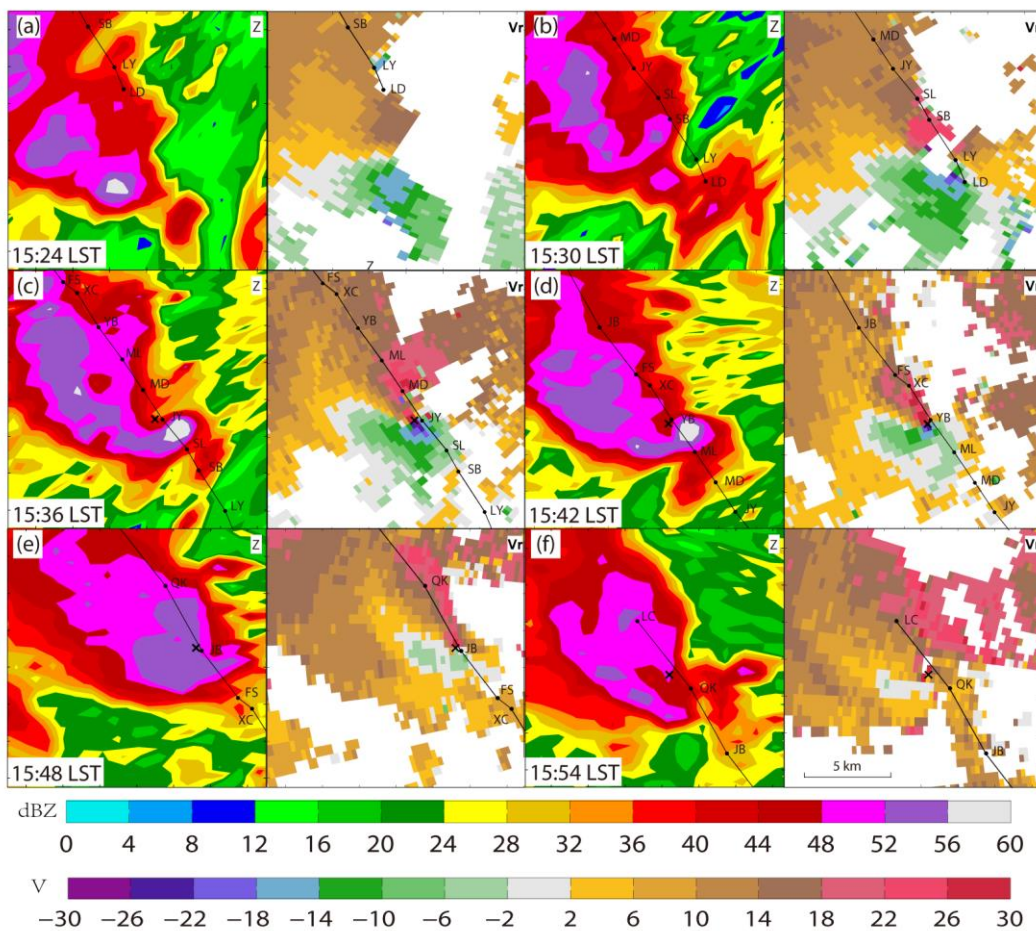
446 barb = 10 m s⁻¹) are also shown. The grey arrow in (b) represents the storm motion.

447



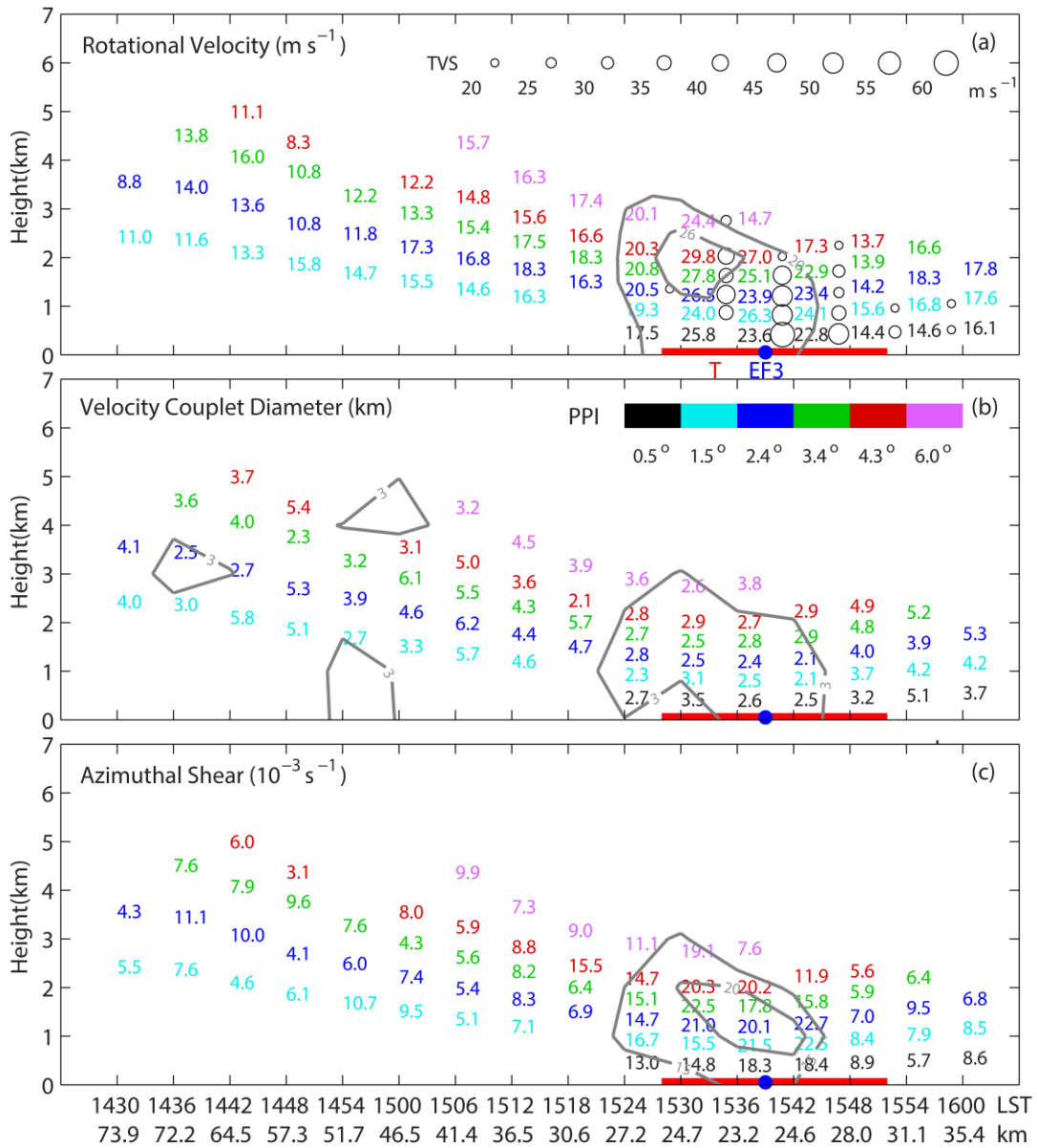
448
 449
 450
 451
 452

Figure 3. Damage survey of tornado path corresponding to the black rectangle in Fig.1. The visual tornado is viewed from the north and the associated damages are illustrated in (b) and (d).



454
 455
 456
 457
 458
 459

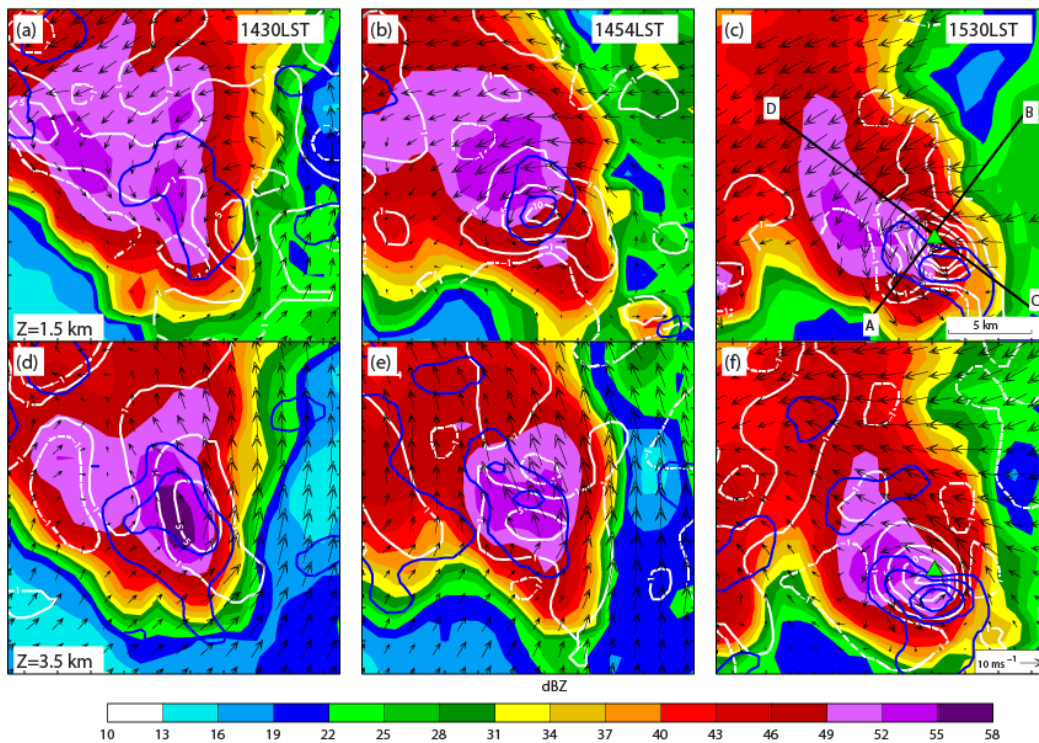
Figure 4. Damage survey of tornado path (solid black line) from Fig. 3 and the TVS (black cross) superimposed on radar reflectivity (dBZ) at 1.5° elevation angle from the Guangzhou radar and ground-relative radial velocities (m s^{-1}) from 1524 to 1554 LST at an interval of 6 min.



460

461 **Figure 5.** Time-height profiles of (a) rotational velocity (m s^{-1}), gray lines represent
 462 20 and 26 m s^{-1} contours, (b) couplet diameter (km), gray lines represent 3 km
 463 contours, and (c) azimuthal shear (10^{-3} s^{-1} , approximately one half of the vertical
 464 vorticity) for the tornado's parent mesocyclone, gray lines represent 15 and 20 $\times 10^{-3}$
 465 s^{-1} contours. A distance scale (km) relative to Guangzhou radar along with the local
 466 time is indicated on the horizontal axis. The strength of the TVS, defined by the
 467 gate-by-gate radial velocity difference is indicated by circles in (a). Colors represent
 468 the elevation angle of PPI scan associated with each quantity. The presence of the
 469 tornado, through visual and damage track records, is indicated by the red line.

470

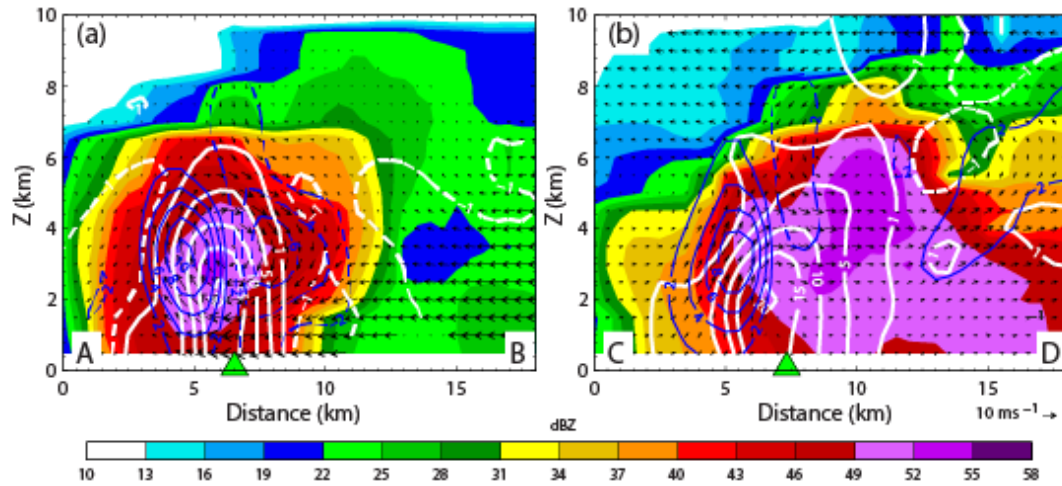


472

473 **Figure 6.** Dual-Doppler analysis of tornadic mesocyclone from Guangzhou and
 474 Shenzhen radars at 1.5 km height (top row) and 3.5 km height (bottom row) at (a,d)
 475 1430 LST, (b,e) 1454 LST and (c,f) 1530 UTC, corresponds to before and at the time
 476 of tornadogenesis. Reflectivity (color, dBZ) is overlaid with storm-relative wind
 477 vectors. The positive (white solid line) and negative (white dashed line) vertical
 478 vorticity is contoured at $\pm 1, 5, 10, 15,$ and $20 \times 10^{-3} \text{ s}^{-1}$. The updraft (blue line)
 479 is contoured at 2, 4, 6, 8, 10 m s^{-1} . The green filled triangles indicate the location of the
 480 TVS.

481

482

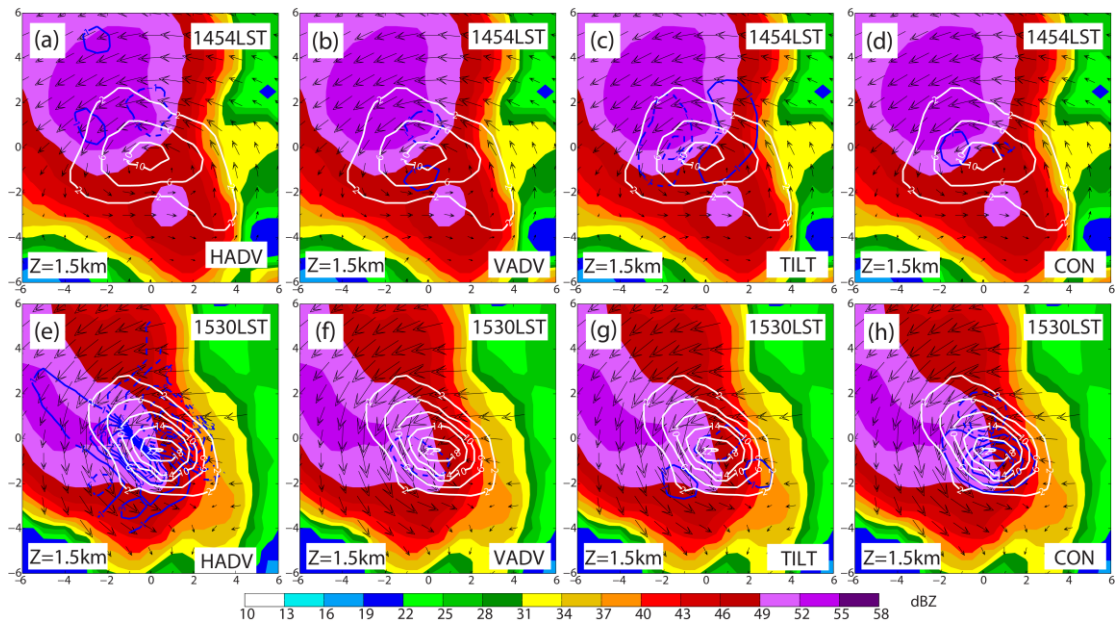


483

484 **Figure 7.** Vertical cross sections of radar reflectivity (dBZ, color shading),
 485 storm-relative wind vectors, vertical velocity (m s^{-1} , blue contours), and vertical
 486 vorticity ($1 \times 10^{-3} \text{ s}^{-1}$, white contours) at 1530 LST (at the time of tornadogenesis)
 487 along (a) AB and (b) CD in Fig. 5c. The solid and dashed lines denote
 488 positive-negative values, respectively. The green filled triangles indicate the location
 489 of TVS.

490

491
492



493

494 **Figure 8.** Distributions of (a,e) HADV, (b,f) VADV, (c,g) TILT, and (d, h) CONV
495 terms within the mesocyclone at 1.5 km at 1454 LST (upper row) and 1530 LST
496 (bottom row), corresponding to the times before and near tornadogenesis. Blue solid
497 (dashed) contours denote positive (negative) contributions to vertical vorticity
498 production with the interval of $2 \times 10^{-6} \text{ s}^{-2}$. Reflectivity (dBZ, color shading) is
499 overlaid with storm-relative wind vectors and vertical relative vorticity (white
500 contours with intervals of $4 \times 10^{-3} \text{ s}^{-1}$).

501
502